Random graphene metasurfaces: diffraction theory and giant broadband absorptivity

Andrey Novitsky[1,2], Alesia Paddubskaya[1], Isaac Appiah Otoo[3], Markku Pekkarinen[3], Yuri Svirko[3], Polina Kuzhir[3]

[1] *Institute for Nuclear Problems of Belarusian State University, Bobruiskaya Str. 11, 220006 Minsk, Belarus*

[2] *Department of Theoretical Physics and Astrophysics, Belarusian State University, Nezavisimosti av. 4, 220030 Minsk, Belarus*

[3] *Department of Physics and Mathematics, Institute of Photonics, University of Eastern Finland, P.O. Box 111, FI-80101 Joensuu, Finland*

Abstract

We introduce diffraction-theory-inspired analytic description of the metasurface comprising an array of graphene subwavelength hemispheres. Our theory describes light interaction with the random metasurface, in which the periodicity is broken by accidentally damaged meta-atoms in the nodes of a two-dimensional periodic lattice. Both numerical modeling and experiment show that such a nm-thin metasurface possesses giant broadband absorption in the THz spectral range that remains intact even when a substantial portion of meta-atoms, i.e. graphene hemispheres, is damaged. Moreover, defective fabrication of graphene free-standing metasurface may enhance the absorptive properties.

Keywords: metasurface, Terahertz, graphene, perfect absorption, diffraction theory

1 Introduction

Tailoring of the surface impedance gave birth to metasurfaces, two-dimensional subwavelength structures capable to control amplitude, phase, and polarization of electromagnetic waves [1-5]. Subwavelength thin metasurfaces outperform volumetric metamaterials heralding their potential use for beam steering and focusing via phase management of the reflected and transmitted waves. This enables numerous applications of metasurfaces including the bandpass and bandstop filters, narrowband perfect absorbers, polarizers, lenses, and holography [2]. The discovery of the phase gradient metasurfaces (also referred to as frequency selective surfaces) capable of control phase in the full range from 0 to 2π has led to the generalization of reflection and refraction laws [6], while metasurfaces comprising spatially varying orientations of subwavelength scatterers enables exploiting the effect of the Pancharatnam-Berry phase [7]. Metasurfaces with long-ranger order in the meta-atoms array can be described in terms of multipole moments (usually dipole moments) of unit cells or equivalent surface impedances. In particular, in so-called Huygens' metasurface [8] the dielectric and magnetic dipole moments of the unit cell arrange in such a way that the reflected wave is suppressed.

Graphene based metasurfaces have attracted attention because control of the graphene surface conductivity (change of the Fermi energy) by chemical or electrical doping may enable tunability in a wide spectral range [9]. Full control of the graphene metasurface can be achieved if the voltage is independently applied to individual unit cells [10]. A graphene metasurface designed to get a $0 - 2\pi$ phase shift due to interplay between plasmon and Fabry-Perot resonances can be employed for cloaking, illusion, and focusing [11]. Curiously, graphene ribbons may act as a

platform for Moiré hyperbolic metasurfaces demonstrating topological transition at magic angles, field canalization, and plasmonic spin-Hall effect [12].

In spite of its negligible thickness the graphene can be used for designing effective absorbers in the THz domain. In Ref. [13], omega-shaped graphene patterns were designed for using as a wide-incident-angle absorber over more than 1 THz band. A wide absorption bandwidth is achievable in a multilayer system with embedded graphene sheet [14], with the perfect absorption for specific incident angle and layer thickness. The broadband absorption in the THz range can also be realized in the planar structures composed of five layers of graphene due to modulation of the graphene chemical potential [15], as well as in singular graphene gratings [16]. Subwavelength periodicity of metasurfaces is advantageous from the fabrication and theoretical modelling perspectives, but not necessary. In this paper, we propose the method of closed-form description of metasurfaces comprising different unit cells randomly distributed on the plane. Such a two-dimensional structure can be called a 'random' metasurface. This term was proposed in Ref. [17] to describe a properties of randomly oriented nanoscale gold bars in the near-infrared frequency range.

Here we investigate random graphene metasurfaces comprising different types of unit cells: hemispheres, volcanos and holes. Assuming that there is no electromagnetic coupling between unit cells we reduce the problem of light interaction with such random metasurfaces to the light scattering by unit cells. We employ the developed approach to the free-standing graphene metasurface and reveal that suppression of meta-atom's dipole moment results in nearly perfect absorption in a wide THz frequency range.

2 Graphene metasurfaces from Kirchhoff diffraction theory viewpoint

We consider a two-dimensional square periodic structure with a period L on the dielectric surface coated with a graphene sheet, which is irradiated with a plane electromagnetic wave at normal incidence (see Fig. 1a for sketch and Figs. 1 b-e for samples experimental realization).
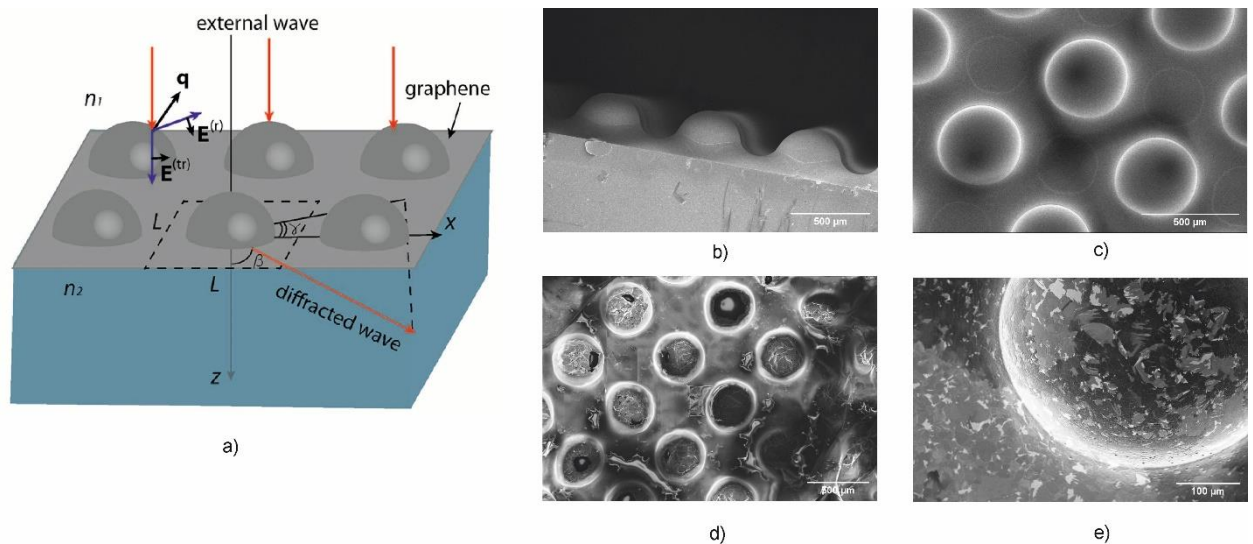

Fig. 1. (a) Sketch of the diffraction by a sculptured graphene sheet separating media with refractive indices n_1 and n_2. (b), (c) SEM images of 3D printed polymer hemispheres on a silica substrate (polymer template). SEM images of the graphene-based metasurface (d), and hemisphere unit cell (e).

Kirchgoff's diffraction theory allows us to present the electromagnetic field in the arbitrary point **r** by the following equation [18]

$$\mathbf{E}(\mathbf{r}) = \int_S \left\{ [\mathbf{n}' \times \mathbf{E}(\mathbf{r}')] \times \nabla' G(\mathbf{r}, \mathbf{r}') + \left(\mathbf{n}' \cdot \mathbf{E}(\mathbf{r}') \right) \nabla' G(\mathbf{r}, \mathbf{r}') + i\omega\mu_0 [\mathbf{n}' \times \mathbf{H}(\mathbf{r}')] G(\mathbf{r}, \mathbf{r}') \right\} ds',$$

(1)

where ω is the wave angular frequency, μ_0 is the vacuum permeability, $\mathbf{n}'$ is the unit vector normal to the surface towards the observation region, and $\nabla' = \partial/\partial\mathbf{r}'$. Vectors $\mathbf{E}(\mathbf{r}')$ and $\mathbf{H}(\mathbf{r}')$ are the electric and magnetic field strengths at the graphene surface S respectively. The scalar Green function

$$G(\mathbf{r}, \mathbf{r}') = \frac{1}{4\pi} \frac{\exp(ik_a|\mathbf{r} - \mathbf{r}'|)}{|\mathbf{r} - \mathbf{r}'|}$$

is determined by the wavenumber $k_a = n_a\omega/c$, where subscript a = 1,2 labels the refractive index at the observation point $\mathbf{r}$.

Equation (1) can be presented in terms of superposition of electromagnetic waves produced by unit cells comprising the surface as

$$\mathbf{E}(\mathbf{r}) = \sum_j \mathbf{E}_j(\mathbf{r}),$$

(2)

where

$$\mathbf{E}_j(r) = \int_{\rho' \in S_j} \left\{ [\mathbf{n}' \times \mathbf{E}(\mathbf{r}')] \times \nabla' G(\mathbf{r}, \mathbf{r}') + \left(\mathbf{n}' \cdot \mathbf{E}(\mathbf{r}') \right) \nabla' G(\mathbf{r}, \mathbf{r}') \right.$$
$$\left. + i\omega\mu_0 [\mathbf{n}' \times \mathbf{H}(\mathbf{r}')] G(\mathbf{r}, \mathbf{r}') \right\} \Big|_{\mathbf{r}' = \rho_j + \rho'} d^2\rho'.$$

(3)

Here integration is taken over area S_j of the jth unit cell having the center situated at point $\boldsymbol{\rho}_j$.

In the Fraunhofer approximation, the distance from the center of the unit cell j to the observation point $r_j = |\mathbf{r} - \boldsymbol{\rho}_j|$ is much greater than the size of the unit cell L, and the Green function and its gradient can be reduced down to

$$G(\mathbf{r}, \mathbf{r}')|_{\mathbf{r}' = \rho_j + \rho'} = \frac{1}{4\pi} \frac{\exp(ik_a r_j)}{r_j}, \quad \nabla' G(\mathbf{r}, \mathbf{r}')|_{\mathbf{r}' = \rho_j + \rho'} = -\frac{ik_a}{4\pi} \frac{\exp(ik_a r_j)}{r_j} \mathbf{m}_j,$$

where $\mathbf{m}_j = \mathbf{r}_j/r_j$. Electric field emitted by the unit cell j equals

$$\mathbf{E}_j(\mathbf{r}) = \frac{ik_a}{4\pi} \frac{\exp(ik_a r_j)}{r_j} \int_{\rho' \in S_j} \left\{ -[\mathbf{n}' \times \mathbf{E}(\mathbf{r}')] \times \mathbf{m}_j - \left(\mathbf{n}' \cdot \mathbf{E}(\mathbf{r}') \right) \mathbf{m}_j \right.$$
$$\left. + Z_a [\mathbf{n}' \times \mathbf{H}(\mathbf{r}')] \right\} |_{\mathbf{r}' = \rho_j + \rho'} d^2\rho',$$

(4)

where $Z_a = \frac{Z_0}{n_a}$ is the wave impedance in the ambient medium, $Z_0 = \sqrt{\mu_0/\varepsilon_0}$ is the vacuum impedance, and ε_0 is the vacuum permittivity.

In order to describe scattering by the metasurface we will assume:

- a normal incidence. In such a case the amplitudes of the electric and magnetic fields at the surface are the same for each unit cell.

- that there is no electromagnetic coupling between neighboring cells, i.e. collective excitations (e.g., surface plasmon-polaritons or surface guided modes) do not occur. In such a case, the light scattered to the medium "1" originates from the wave reflected from the metasurface, while the wave scattered into the medium "2" originates from the transmitted wave. In order to find the electric filed strength in media "1" ("2"), we can replace $\mathbf{E}(\mathbf{r}')$ and $\mathbf{H}(\mathbf{r}')$ in Eq. (4) with electric and magnetic fields, respectively, of the wave reflected from (transmitted through) metasurface at the point $\mathbf{r}'$ of the unit cell. Therefore, by taking into account the geometry and material properties of individual cells and summing up contributions of all unit cells we will obtain the reflectance and transmittance of the metasurface.

Equation (4) is valid for an arbitrary unit cell geometry, however it can be considerably simplified for unit cells of high symmetry. In particular, it can be shown that if the unit cell possesses a cylindrical symmetry with respect to the propagation direction of the incident wave, the following relationships hold:

$$\int_{S_c} \left(\mathbf{n}' \cdot \mathbf{E}(\mathbf{r}')\right) d^2 r' = 0, \qquad Z_a \int_{S_c} [\mathbf{n}' \times \mathbf{H}(\mathbf{r}')] d^2 r' = \mathbf{e}_z \times \int_{S_c} [\mathbf{n}' \times \mathbf{E}(\mathbf{r}')] \, d^2 r', \qquad (5)$$

where S_c is the unit cell area. In the absence of coherency between identical unit cells (no Bragg diffraction), the metasurface spectral properties can be described by the single unit cell with averaged characteristics and the normalized power scattered to the solid angle $do = \sin \beta \, d\beta d\gamma$ towards the medium "1" ($\pi/2 < \beta < \pi$)

$$\frac{dP^{(1)}}{do}(f, \beta, \gamma) = \frac{\left|\mathbf{I}^{(1)}(f,\beta,\gamma)\right|^2 \cos \beta}{|\mathbf{E}_i|^2 \, L^4} \tag{6}$$

and medium "2" ($0 < \beta < \pi/2$)

$$\frac{dP^{(2)}}{do}(f, \beta, \gamma) = \frac{n_2 \left|\mathbf{I}^{(2)}(f,\beta,\gamma)\right|^2 |\cos \beta|}{n_1 |\mathbf{E}_i|^2 \, L^4} \tag{7}$$

where f is the wave frequency. Angles β and γ are introduced in Fig. 1a. Vectors

$$\mathbf{I}^{(1)} = \int_{S_c} [\mathbf{n}' \times \mathbf{E}_r(\mathbf{r}')] \, d^2 r', \qquad \mathbf{I}^{(2)} = \int_{S_c} [\mathbf{n}' \times \mathbf{E}_t(\mathbf{r}')] \, d^2 r' \tag{8}$$

are determined by the distribution of the reflected $\mathbf{E}_r(\mathbf{r}')$ and transmitted $\mathbf{E}_t(\mathbf{r}')$ electric field over the unit cell area.

Reflection and transmission coefficients for the TE and TM (with respect to the element of the unit cell surface) polarized components of the incident wave are equal to

$$r_{TE}(\alpha_1) = \frac{n_1 \cos \alpha_2 - (n_2 + \sigma Z_0 \cos \alpha_2) \cos \alpha_1}{n_1 \cos \alpha_2 + (n_2 + \sigma Z_0 \cos \alpha_2) \cos \alpha_1}, \qquad r_{TM}(\alpha_1) = \frac{n_1 \cos \alpha_1 - (n_2 \cos \alpha_2 + \sigma Z_0)}{n_1 \cos \alpha_1 + (n_2 \cos \alpha_2 + \sigma Z_0)},$$

$$t_{TE}(\alpha_1) = \frac{2 n_1 \cos \alpha_2}{n_1 \cos \alpha_2 + (n_2 + \sigma Z_0 \cos \alpha_2) \cos \alpha_1}, \qquad t_{TM}(\alpha_1) = \frac{2 n_1 \cos \alpha_1}{n_1 \cos \alpha_1 + (n_2 \cos \alpha_2 + \sigma Z_0)}, \tag{9}$$

where σ is the graphene surface conductivity, while α_1 and $\alpha_2 = \arcsin(n_1 \sin \alpha_1 / n_2)$ are the local angle of incidence and refraction, respectively. The transmissivity and reflectivity of the metasurface can be obtained by calculating the total energy diffracted into media "1" and "2", respectively, as

$$T(f) = \int_0^{\frac{\pi}{2}} \int_0^{2\pi} \frac{dP^{(2)}}{do}(f,\beta,\gamma) \sin\beta \, d\beta \, d\gamma \,, \quad R(f) = \int_{\pi/2}^{\pi} \int_0^{2\pi} \frac{dP^{(1)}}{do}(f,\beta,\gamma) \sin\beta \, d\beta \, d\gamma. \quad (10)$$

3 Unit cells of cylindrical symmetry

We have demonstrated [19] that a complex fabrication procedure of graphene metasurface involving 3D printing, electroplating, graphene synthesis and transfer allows a plenty of room for introducing imperfections to the meta-atoms structure. In particular, in the fabricated array of graphene hemispheres with the characteristic size of 200-600 microns, a considerable proportion of hemispheres may be completely or partially damaged being either holes or volcano-like structures, respectively (see Figs. 1d-e for fabricated samples and Fig.2 for sketch). Below we will calculate the reflectance and transmittance of the metasurface comprising such cylindrically symmetric unit cells assuming normal incidence.

3.1 Hole-type unit cell

The hole-type unit cell, i.e. a hole of radius R in the center of the flat graphene sheet of size $L \times L$, is shown in Fig. 2a. For the reflected (transmitted) wave, the normal vector of the flat sheet reads $\mathbf{n}' = -\mathbf{e}_z$ ($\mathbf{n}' = \mathbf{e}_z$). In order to calculate $\mathbf{I}^{(1)}$ in Eq. (8) we need to take into account that the graphene-covered and graphene free areas of the unit cell are $S_{gr} = L^2 - \pi R^2$ and $S_h = \pi R^2$, respectively, and there is a phase shift owing to the oblique propagation of the diffracted wave propagating in the direction defined by the spherical angles (β,γ). For the wave diffracted to the medium "1" this gives $\mathbf{I}_{hole}^{(1)} = \mathbf{I}^{(1,hl)} + \mathbf{I}^{(1,fl)}$, where

$$\mathbf{I}^{(1,hl)}(\beta) = -r_0 \frac{2\pi R}{n_1 k_0 \sin\beta} J_1(n_1 k_0 R \sin\beta)[\mathbf{e}_z \times \mathbf{E}_i],$$

$$\mathbf{I}^{(1,fl)}(\beta,\gamma) = -r_g \left\{ \frac{8 \sin\left(\frac{n_1 k_0 L}{2}\cos\gamma \sin\beta\right) \sin\left(\frac{n_1 k_0 L}{2}\sin\gamma \sin\beta\right)}{(n_1 k_0 \sin\beta)^2 \sin 2\gamma} - \frac{2\pi R}{n_1 k_0 \sin\beta} J_1(n_1 k_0 R \sin\beta) \right\} [\mathbf{e}_z \times \mathbf{E}_i].$$

$$(11)$$

Here $r_g = \frac{n_1 - (n_2 + \sigma Z_0)}{n_1 + (n_2 + \sigma Z_0)}$ and $r_0 = \frac{n_1 - n_2}{n_1 + n_2}$ are reflection coefficients of the graphene-covered and graphene-free areas, respectively, at normal incidence and $J_1(x)$ is the Bessel function of the 1st order.

Similarly, for the wave diffracted to the medium "2" we arrive at

$$\mathbf{I}^{(2,hl)}(\beta) = t_0 \frac{2\pi R}{n_2 k_0 \sin\beta} J_1(n_2 k_0 R \sin\beta)[\mathbf{e}_z \times \mathbf{E}_i]$$

$$\mathbf{I}^{(2,fl)}(\beta,\gamma) = t_g \left\{ \frac{8 \sin\left(\frac{n_2 k_0 L}{2}\cos\gamma \sin\beta\right) \sin\left(\frac{n_2 k_0 L}{2}\sin\gamma \sin\beta\right)}{(n_2 k_0 \sin\beta)^2 \sin 2\gamma} - \frac{2\pi R}{n_2 k_0 \sin\beta} J_1(n_2 k_0 R \sin\beta) \right\} [\mathbf{e}_z \times \mathbf{E}_i],$$

$$(12)$$

where $t_g = \frac{2n_1}{n_1 + (n_2 + \sigma Z_0)}$ and $t_0 = \frac{2n_1}{n_1 + n_2}$ are transmission coefficients of the graphene-covered and graphene-free areas, respectively, at normal incidence.

Equations (11,12) allow us to obtain the reflectance R_n and transmittance T_n in the direction normal to the graphene sheet as

$$R_n(f) = \frac{dP^{(1)}}{do}(f, \pi, 0) = \left| r_g + (r_0 - r_g)\frac{\pi R^2}{L^2} \right|^2$$

$$T_n(f) = \frac{dP^{(2)}}{do}(f, 0, 0) = \left| t_g + (t_0 - t_g)\frac{\pi R^2}{L^2} \right|^2 \qquad (13)$$

When $\sigma Z_0 \ll n_1 = n_2$, the reflectivity coefficient $r_0 = 0$, while $r_g \approx \sigma Z_0/2n_1$ is low and shows a weak frequency dispersion determined by the Drude-like formula for graphene surface conductivity [20]

$$\sigma = \frac{\sigma_0}{1 + i\omega\tau}, \qquad (14)$$

where $\sigma_0 = e^2 E_F \tau / \pi \hbar^2$ is the static conductivity, $\tau = \mu \hbar \sqrt{n_s \pi}/e v_F$ is the carrier relaxation time, $n_s = E_F^2/\pi \hbar^2 v_F^2$, μ is the carrier mobility, E_F is the Fermi energy, and v_F is the Fermi velocity. Figure 2g shows that reflected power is small, while the transmitted power maximizes for normally diffracted wave at $\beta = 0$.
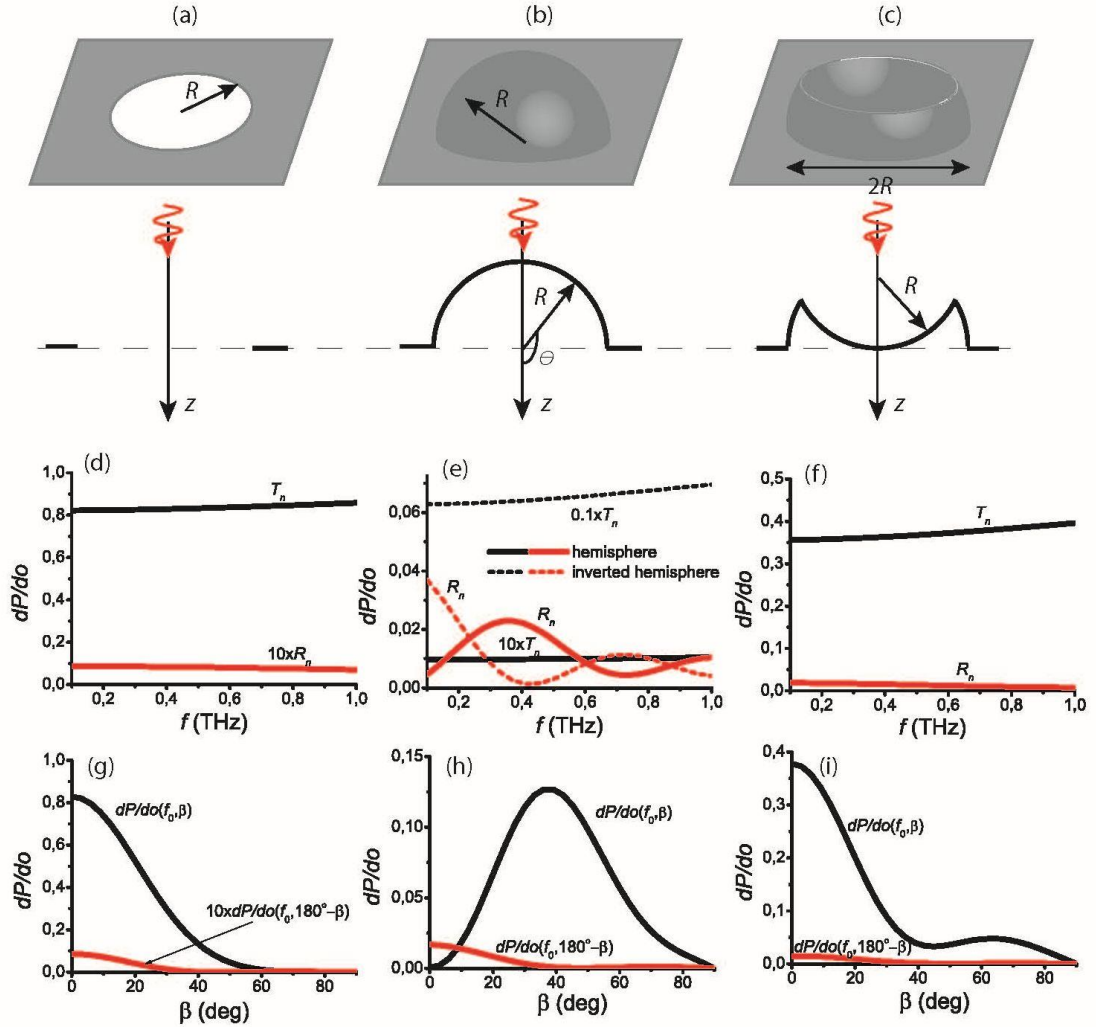

Fig. 2. Power scattered by the metasurface per solid angle $\frac{dP}{do}(f, \beta, 0)$ for (a,d,g) hole-type, (b,e,h) hemisphere-type, and (c,f,i) volcanic-type unit cells. Drude-model parameters of graphene are $\mu = 1\ \mathrm{m^2/V}$, $E_F = 0.1$ eV, $v_F = 10^6$ m/s; geometrical parameters of the metasurface are $L =$

611 μm and $R = 250$ μm; refractive indices of the ambient media are $n_1 = n_2 = 1$; frequency $f_0 = 0.5$ THz. Unit cell cross-sections are shown in the lower parts of figures (a-c).

3.2 Hemisphere-type unit cell

Hemisphere-type unit cell comprises a graphene hemisphere of radius R in the center of the flat graphene square $L \times L$ (see Fig. 2b). The wave diffracted into medium "1" is described by $\mathbf{I}_{hemi}^{(1)} = \mathbf{I}^{(1,fl)} + \mathbf{I}^{(1,hs)}$, where $\mathbf{I}^{(1,fl)}$ was introduced in Eq. (11) and

$$\mathbf{I}^{(1,hs)}(\beta) = -R^2 \int_{\frac{\pi}{2}}^{\pi} \int_0^{2\pi} [\mathbf{e}_r(\theta,\varphi) \times \hat{r}(\pi - \theta)\mathbf{E}_i]e^{i\psi_1(\theta,\beta)} \sin\theta \, d\theta d\varphi, \tag{15}$$

Here $\frac{\pi}{2} \leq \theta \leq \pi$ and $0 \leq \varphi < 2\pi$ describe the surface of the hemisphere with radius R as illustrated in Fig. 2b, $\mathbf{n}' = \mathbf{e}_r(\theta,\varphi)$ is the unit vector of the outward normal of the hemisphere, and $\hat{r}(\theta) = \text{diag}\{r_{TE}(\theta), r_{TM}(\theta)\}$ is the reflection coefficient matrix. $\psi_1(\theta,\beta) = n_1 k_0 R[\cos\theta + \cos(\theta - \beta)]$ accounts for a phase of the wave diffracted at the azimuthal angle β with respect to the plane $z=0$. Owing to the rotational symmetry, the integral $\mathbf{I}^{(1,hs)}$ is γ independent.

Electric field of the wave diffracted into medium "2" is provides a relationship $\mathbf{I}_{hemi}^{(2)} = \mathbf{I}^{(2,fl)} + \mathbf{I}^{(2,hs)}$, where $\mathbf{I}^{(2,fl)}$ was introduced in Eq. (12) and

$$\mathbf{I}_1^{(2,hs)}(\beta) = R^2 \int_{\pi/2}^{\pi} \int_0^{2\pi} [\mathbf{e}_r(\theta,\varphi) \times \hat{t}(\pi - \theta)\mathbf{E}_i]e^{i\psi_2(\theta,\beta)} \sin\theta \, d\theta d\varphi. \tag{16}$$

Here we take into account that for the transmitted wave $\mathbf{n}' = -\mathbf{e}_r(\theta,\varphi)$, $\hat{t}(\theta) = \text{diag}\{t_{TE}(\theta), t_{TM}(\theta)\}$, and the phase shift $\psi_2(\theta,\beta) = k_0 R[n_2 \cos(\theta - \beta) - n_1 \cos\theta]$.

One can see from Fig. 2(e) that at $\beta = 0$ both normal reflectance $R_n(f) = \frac{dP^{(1)}}{do}(f,0,0)$ and normal transmittance $T_n(f) = \frac{dP^{(2)}}{do}(f,0,0)$ of the hemisphere unit cell are very small. The negligible normal transmissivity can be understood, if one considers that the diffracted field along z-axis originates from the projection $\mathbf{p}_\parallel$ on the XY-plane of the net dipole moment induced in the graphene by the incident wave. The effective in-plane dipole moment of the unit cell can be presented in the following form:

$$\mathbf{p}_c = \int_{L \times L} \mathbf{p}_\parallel \, e^{i\Delta\psi(x',y')} \frac{dx'dy'}{L^2}, \tag{17}$$

where the phase shift $\Delta\psi$ takes into account the distance between the hemisphere surface and plane $z=0$. By introducing amplitude of the surface current density $\mathbf{j}_s = -i\omega\mathbf{p}_\parallel$ oscillating at frequency ω and taking into account that $\mathbf{j}_s = \sigma\mathbf{E}(x',y')$, the dipole moment of the unit cell can be presented in terms of the incident light filed as

$$\mathbf{p}_c = \frac{i\sigma_s}{\omega L^2} \int_{L \times L} \hat{t}(x',y')\mathbf{E}_i \, e^{i\Delta\psi(x',y')} \, dx'dy'. \tag{18}$$

Here $\hat{t}(x',y') = \text{diag}\{t_{TE}(x',y'), t_{TM}(x',y')\}$ is the transmission coefficient of the graphene at point (x',y') of the unit cell.

Figure 3a shows the dependence of $|\mathbf{p}_c|$ on the radius R of holes (black solid line) and hemispheres (red solid line). At small R, the effective dipole moments of both types of unit cells are approximately equal and close to the dipole moment of the flat graphene. Dipole moments

decrease with radius, the dependence being not monotonous for hemispheres. Specifically, for the graphene hemisphere, the dipole moment is minimal at $R=265$ μm. In such a hemisphere, $|\mathbf{p}_c|$ does not exceed ten percent of the dipole moment generated in the hole-type unit cells with the same hole radius. This is because the surface current density in the flat graphene area and projection of the current density on the hemisphere surface to the plane z=0 are anti-parallel as demonstrated in Fig. 3b. If we further increase the radius R, then the dipole moment of the hemisphere prevails and the absolute value of the net dipole moment increases again as it can be seen from Fig. 3a.
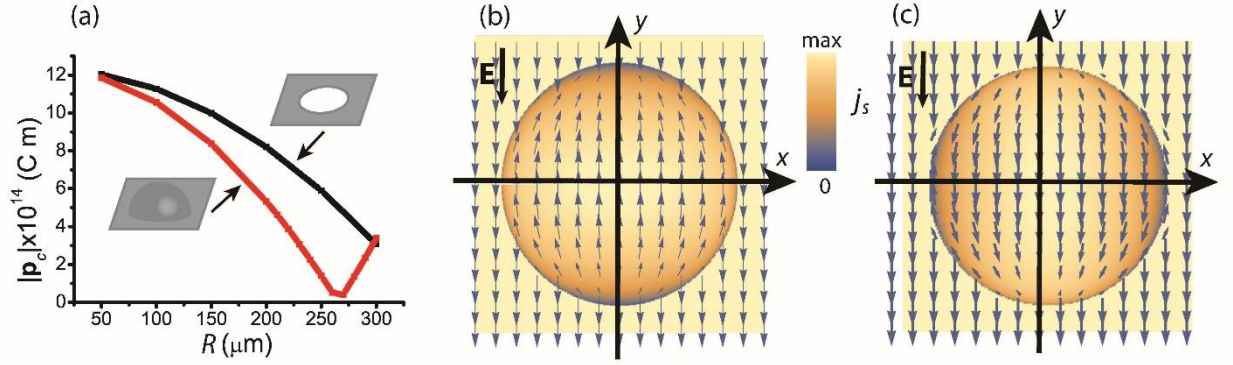

Figure 3. (a) Absolute value of unit cell's dipole moment $|\mathbf{p}_c|$ as function of the radius R of either holes or hemispheres. Distribution of the current density j_s projected onto the plane z=0 for (b) hemispherical and (c) volcanic unit cells. Parameters are as in Fig. 2.

Hemisphere inverted with respect to the plane z=0 exhibits dramatically different properties. In this case, the hemisphere is described by $0 \leq \theta \leq \pi/2$, while the normal vector $\mathbf{n'} = -\mathbf{e}_r(\theta, \varphi)$ corresponds to the wave diffracted into the medium "1" yielding

$$\mathbf{I}_{inv}^{(1,hs)}(\beta) = -R^2 \int_0^{\frac{\pi}{2}} \int_0^{2\pi} [\mathbf{e}_r(\theta, \varphi) \times \hat{r}(\theta) \mathbf{E}_i] e^{i\psi_1(\theta, \beta)} \sin \theta \, d\theta d\varphi. \tag{19}$$

It worth mentioning that the phase function $\psi_1(\theta, \beta)$ does not change.

Normal transmittance T_n and reflectance R_n of the metasurface with inverted hemispheres are demonstrated in Fig. 2e with dashed lines. The magnitudes of R_n are comparable for hemispheres and their inverted counterparts, but the maxima and minima change over. At the same time the value T_n significantly increases, more than 100 times compared to the case of normal hemispheres.

Although normal transmittance T_n is very low for hemispheres, the scattered power to the medium "2" can be quite large. From Fig. 2h one can observe that the scattered power is maximal near $\beta = 40°$ indicating that considerable light energy can be diffracted at nonzero angles, while the reflected power, which is determined by the graphene surface conductivity, remains small for all diffraction angles.

3.3 Volcanic-type unit cell

The third type of the unit cell we consider is a broken hemisphere, in which upper segment falls down forming a sort of volcano crater as shown in Fig. 2c. The volcano-like shape is composed of

two segments. The first one, $\pi/2 \le \theta \le 2\pi/3$, is a remainder of the initial hemisphere characterized by the normal vector $\mathbf{n}' = \mathbf{e}_r$ for the waves diffracted to the medium "1". The second segment, $0 \le \theta \le \pi/3$, is a part of the sphere centered at $z = -R$, its normal vector is $\mathbf{n}' = -\mathbf{e}_r$. Thus, the integral describing diffraction to the medium "1" reads $\mathbf{I}_{volcano}^{(1)} = \mathbf{I}^{(1,fl)} + \mathbf{I}^{(1,vol)}$, where

$$\mathbf{I}^{(1,vol)}(\beta) = R^2 \int_{\pi/2}^{2\pi/3} \int_0^{2\pi} [\mathbf{e}_r(\theta, \varphi) \times \hat{r}(\pi - \theta)\mathbf{E}_i] e^{i\psi_1(\theta,\beta)} \sin\theta \, d\theta d\varphi$$

$$- R^2 \int_0^{\frac{\pi}{3}} \int_0^{2\pi} [\mathbf{e}_r(\theta, \varphi) \times \hat{r}(\theta)\mathbf{E}_i] e^{i\psi_1(\theta,\beta)-2ikR} \sin\theta \, d\theta d\varphi.$$

(20)

For calculation of the transmittance, we need to reverse the normal vector $\mathbf{e}_r(\theta, \varphi) \to -\mathbf{e}_r(\theta, \varphi)$ and replace $\psi_1(\theta, \beta)$ and $\psi_1(\theta, \beta) - 2kR$ with $\psi_2(\theta, \beta)$.

Dependences of the scattered power on the frequency and diffraction angle are quite similar to those for the hole-type metasurface, compare Fig. 2d and Fig. 2f, and Fig. 2g and Fig.2i. However, the magnitudes of the scattered power are lower for volcano craters. Distribution of the forward scattered power in Fig. 2i has an intensive tail for $\beta > 40°$. The enhanced scattering of volcanic-type metasurfaces are supported by the distribution of the current density in Fig. 3c showing that in this case, the dipole moment of the unit cell gives rise to the high transmissivity.

4 Random metasurfaces

Inevitable fabrication defects break long-range order in the 2D array of meta-atoms and may essentially affect the performance of the metasurface. In this section, we will estimate at what extent the hole- and volcano-type defects are capable to affect the diffracted field. Specifically, we assume that the probabilities of finding the undamaged hemisphere, hole-type defect and volcano-type defect in particular position of the meta-atoms array are w_1, w_2, and w_3, respectively, where $w_1 + w_2 + w_3 = 1$. In such a case the reflectivity can be found by averaging electric field scattered by the meta-atoms into the medium "1", i.e. by replacing $\mathbf{I}^{(1)}(f, \beta, \gamma)$ in Eq. (6) with

$$\langle \mathbf{I}^{(1)} \rangle = w_1 \mathbf{I}_{hemi}^{(1)} + w_2 \mathbf{I}_{hole}^{(1)} + w_3 \mathbf{I}_{volcano}^{(1)}. \tag{21}$$

Since each unit cell also includes flat graphene-covered substrate, we can present the energy diffracted into medium "1" in terms of the integrals introduced in the previous section as

$$\langle \mathbf{I}^{(1)} \rangle = w_1 \left[\mathbf{I}^{(1,fl)} + \mathbf{I}^{(1,hs)} \right] + w_2 \left[\mathbf{I}^{(1,fl)} + \mathbf{I}^{(1,hl)} \right] + w_3 \left[\mathbf{I}^{(1,fl)} + \mathbf{I}^{(1,vol)} \right]$$

$$= w_1 \mathbf{I}^{(1,hs)} + w_2 \mathbf{I}^{(1,hl)} + w_3 \mathbf{I}^{(1,vol)} + \mathbf{I}^{(1,fl)}.$$

(22)

In order to find the power diffracted into medium "2" we should change the superscript 1 to 2, i.e. $\mathbf{I}^{(1,hs)} \to \mathbf{I}^{(2,hs)}$ and so on.

In the following analysis we assume $w_1 = 0.6$, $w_2 = 0.35$, and $w_3 = 0.05$, which corresponds to the metasurface studied in [19]. Comparing the results of modeling presented in Fig. 4a with

those in Figs. 2d-f one may conclude that, at $\beta = 0°$, the hemisphere-type unit cells dominate the transmittance and reflectance of the random metasurface. Our analysis shows that relative contribution of volcano- and hole-type unit cells essentially depends on frequency. The angular dependences in Fig. 4b allow one to notice characteristic peaks featuring contributions of a particular type of unit cell, which responses are given in Figs. 2g-i. At $f_0 = 0.5$ THz, we see the contribution of the volcano-type unit cell as a maximum at $\beta = 0°$ and the contribution of the hemisphere-type unit cell as a feeble peak near $\beta = 40°$.

Spectra of the reflectivity and transmissivity calculated using Eq. (10), i.e. the total relative power scattered to the medium "1" and "2", are illustrated in Fig. 5. While the reflectivity is low in the whole frequency range, the transmissivity increases up to 18% at 0.1 THz because $\frac{dP^{(2)}}{do}(f,\beta,\gamma)$ increases when frequency decreases (see Fig. 4b). The absorptivity $A = 1 - R - T$ of the graphene metasurface exceeds 80% in the spectral range from 0.1 to 1 THz and 90% from 0.5 to 1 THz being as high as 94% at 1 THz. Such a strong absorption performance is surprising accounting for a noticeable proportion of the damaged meta-atoms that destroys the low-range order in the array. It is important that the considered random metasurface is a broadband absorber due to the suppressed dipole moment and, therefore, transmissivity.

It is worth noting that transmittance and reflectance for the wave diffracted normally to the metasurface, $T_n(f) = \frac{dP^{(2)}}{do}(f,0,0)$ and $R_n(f) = \frac{dP^{(1)}}{do}(f,0,0)$, respectively, can be used for a reasonable estimation of the absorptivity according to $A \approx 1 - T_n - R_n$ (see Fig. 5). In the case of oblique incidence, the reflectivity stays small due to low graphene's conductivity, while the transmissivity may significantly increase owing to essential dipole moment of the unit cell, thus ruining high absorptivity of the graphene random metasurface.
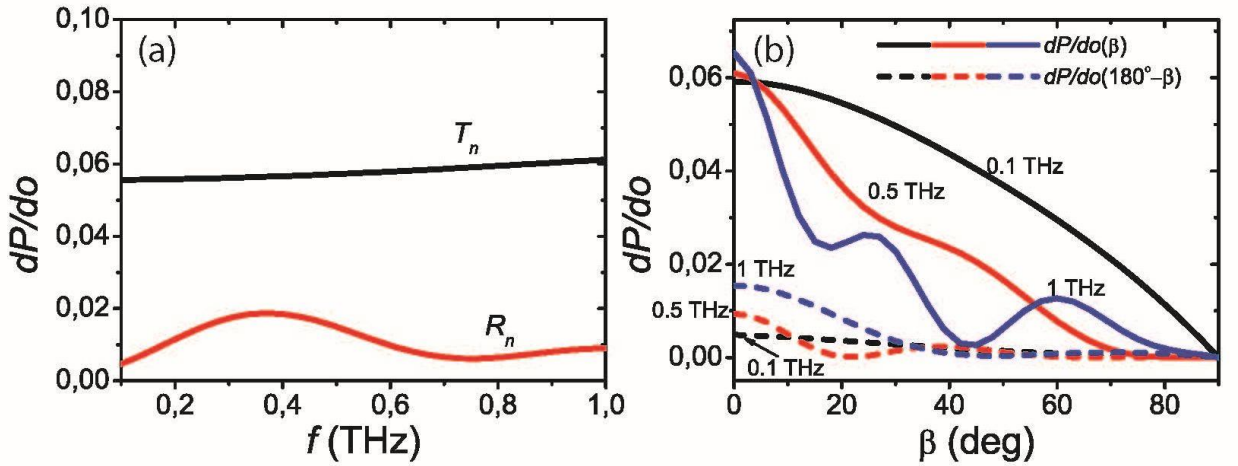

Figure 4. (a) Power scattered normally to the metasurface in the forward T_n and backward R_n directions. (b) Power $\frac{dP}{do}$ scattered by the metasurface over the whole range of diffraction angles for 3 frequencies $f_0 = 0.1; 0.5; 1$ THz. Parameters of the unit cells are given in Fig. 2, while the weight factors are $w_1 = 0.6$, $w_2 = 0.35$, and $w_3 = 0.05$.
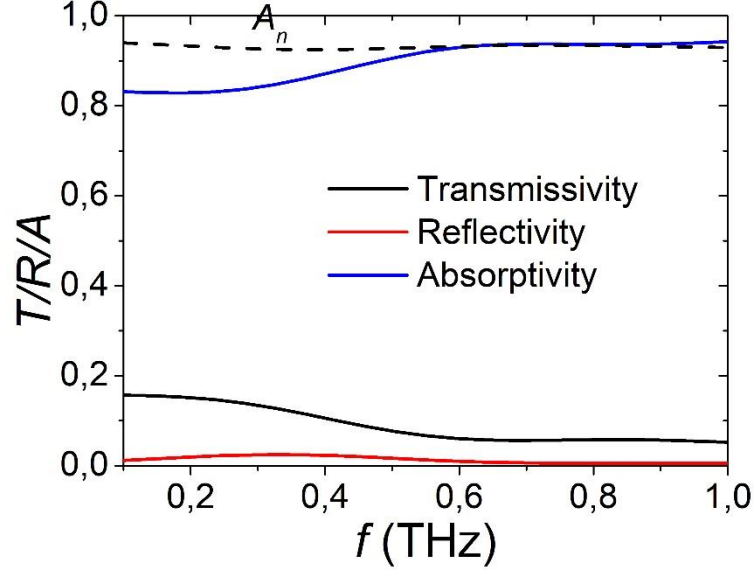
Figure 5. Reflectivity, transmissivity, and absorptivity of the random metasurface in Fig. 4. The dashed line demonstrates the absorptivity calculated as $A_n = 1 - T_n - R_n$.

5 Results and Discussion

5.1. Comparison to experiment

The samples of free-standing metasurface composed of graphene hemispheres have been fabricated as described in [19], see Figs. 1b-e. Briefly, 3D printed array of the polymer hemispheres was sputtered by nm-thick Ni layer for further electroplating to fabricate nickel pattern used for CVD synthesis of multilayered graphene. Graphene metasurface was then coated with 200 nm of polymethylmethacrylate (PMMA) for safe transfer to the membrane holder.

The metasurface is typically composed of 55-60% of ideal hemisphere ($w_1 = 0.6$), 30-40 % of volcano ($w_2 = 0.35$), and 5-10% of hole ($w_3 = 0.05$) meta-atoms.

The details of the THz time domain set-up and THz measurements can be found in [22].

In order to compare results of the experiment with predictions of the developed model we take into account that the PMMA film thickness is much smaller than the wavelength, i.e. we may consider graphene metasurface in the free space ($n_1 = n_2 = 1$). In order to account piecewise nature of multi-layered graphene made on electroplated Ni template [19], comprising single and two-layers graphene domains, we will modify Eq. (14) for the surface conductivity as follows

$$\sigma_s^{eff} = Y \frac{\sigma_0}{1+i\omega\tau}, \tag{23}$$

where $Y = \alpha_1 + 2\alpha_2$, α_1 and α_2 are the weight factors of the single-layer and two-layers graphene areas ($\alpha_1 + \alpha_2 = 1$).

Figure 6 shows measured and calculated dependences of the diffracted power on the frequency and diffraction angle. One can observe from Fig. 6a that theory reproduces the measured transmittivity with about 20% accuracy in the whole spectrum range. Figures 6b-d demonstrate

that the modelling catches a general trend in the dependence of $\frac{dP^{(2)}}{do}(\beta)$ on the diffraction angle β, what can serve as a validation of the applied averaging procedure on the geometry of unit cells.
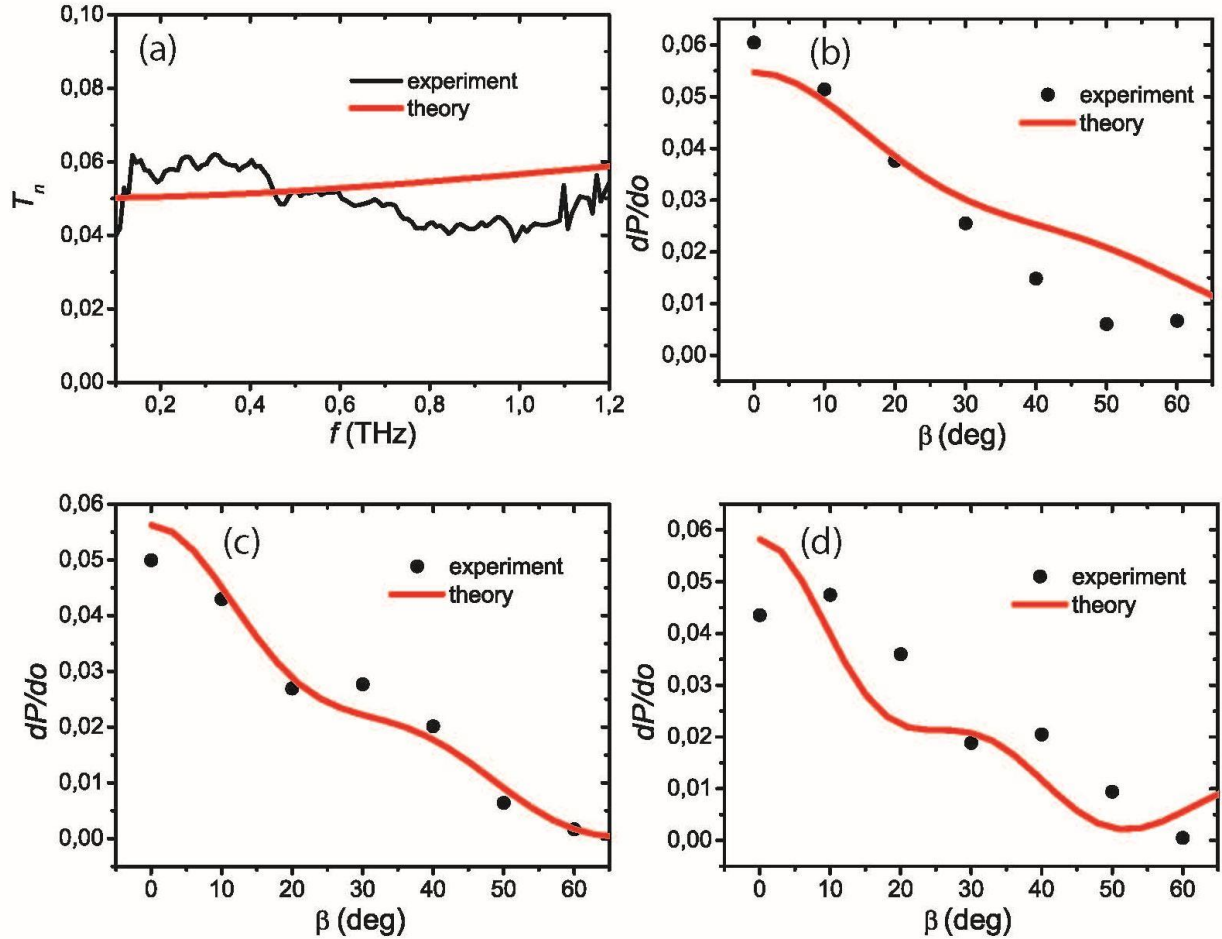

Figure 6. Frequency dependence of the metasurface normal transmittance (a) and scattered power $\frac{dP^{(2)}}{do}$ vs. diffraction angle β at (b) 0.4 THz, (c) 0.6 THz, and (d) 0.8 THz. Solid red lines represent predictions of the developed theory, while black solid line and black dots show experimental data. Metasurface parameters are shown in the caption of Fig. 4. Graphene surface conductivity was calculated from Eq.(23) assuming the layering weight factors $\alpha_1 = 0.7$ and $\alpha_2 = 0.3$.

5.2 Absorptivity optimization

In this subsection, we will investigate the influence of all parameters (graphene conductivity, metasurface geometry and perfectness) on the metasurface absorptivity A, which is of a paramount practical importance. One can see from Fig. 7a that in order to increase absorptivity one need to reduce the Fermi energy, i.e. the doping level of graphene should be moderate. In such a case, the surface conductivity and reflectivity will be low, whereas the transmissivity can be suppressed due to tailoring of the unit cells geometry. For higher Fermi energies, the conductivity and reflectivity increase, while the transmissivity decreases leading to suppressing

of the absorptivity. Therefore, typical for CVD graphene/PMMA sandwich [22] Fermi energy of $E_F = 0.1$ eV, is appropriate to achieve a high absorptivity.

The absorptivity as a function of the frequency demonstrated in Fig. 5 indicates the higher the frequency, the higher the absorptivity. Figure 7b shows that the absorptivity is very close to the perfect one at $f > 5$ THz. At high frequencies the transmissivity peaks in the vicinity of $\beta = 0$ (geometrical optics limit), i.e. the transmittivity coincides with the transmittance at normal incidence, $T \approx T_n$, and, therefore, the absorptivity is well estimated by $A \approx A_n$. Further, we fix the value of the frequency $f_0 = 0.5$ THz and determine the maximal value of the absorptivity $A(R, w_1)$ as a function of these two parameters.

Figure 7c presents a map of the absorptivity as a function of hemisphere radius R and proportion of the perfect hemispheres in the array, w_1. At small radii R, the dipole moment of the meta-atom does not vanish and, therefore, the transmissivity is noticeable. At bigger radii, the dipole moment and transmissivity can be minimized at some value of w_1, thus maximizing the absorptivity. The default parameters ($w_1 = 0.6$ and $R = 250\ \mu$m) marked with a circle in the figure are within the region of high absorptivity A>0.8 highlighted by the dashed line in Fig. 7c. Figure 7d shows the density plot of the absorptivity as a function f and w_1 at hemisphere radius $R = 250\ \mu$m. One can see that the absorptivity is high in a wide range of w_1 and f and rapidly decreases at lower frequencies.

There are no strict limitations on the spacing between unit cells L, because the effect of near-perfect absorptivity is irrelevant to resonances. The frequency window, in which the metasurface absorber works, is restricted by the increase of graphene's conductivity and, therefore, reflectivity at lower frequencies and influence of interband transitions at higher frequencies. According to Ref. [23] the intraband contribution dominates over the interband one for the wavelengths greater than approximately 30 μm, what is equivalent to frequencies $f < 10$ THz. The Drude model for graphene can be applied only up to this frequency showing a high absorptivity in Fig. 7(b).
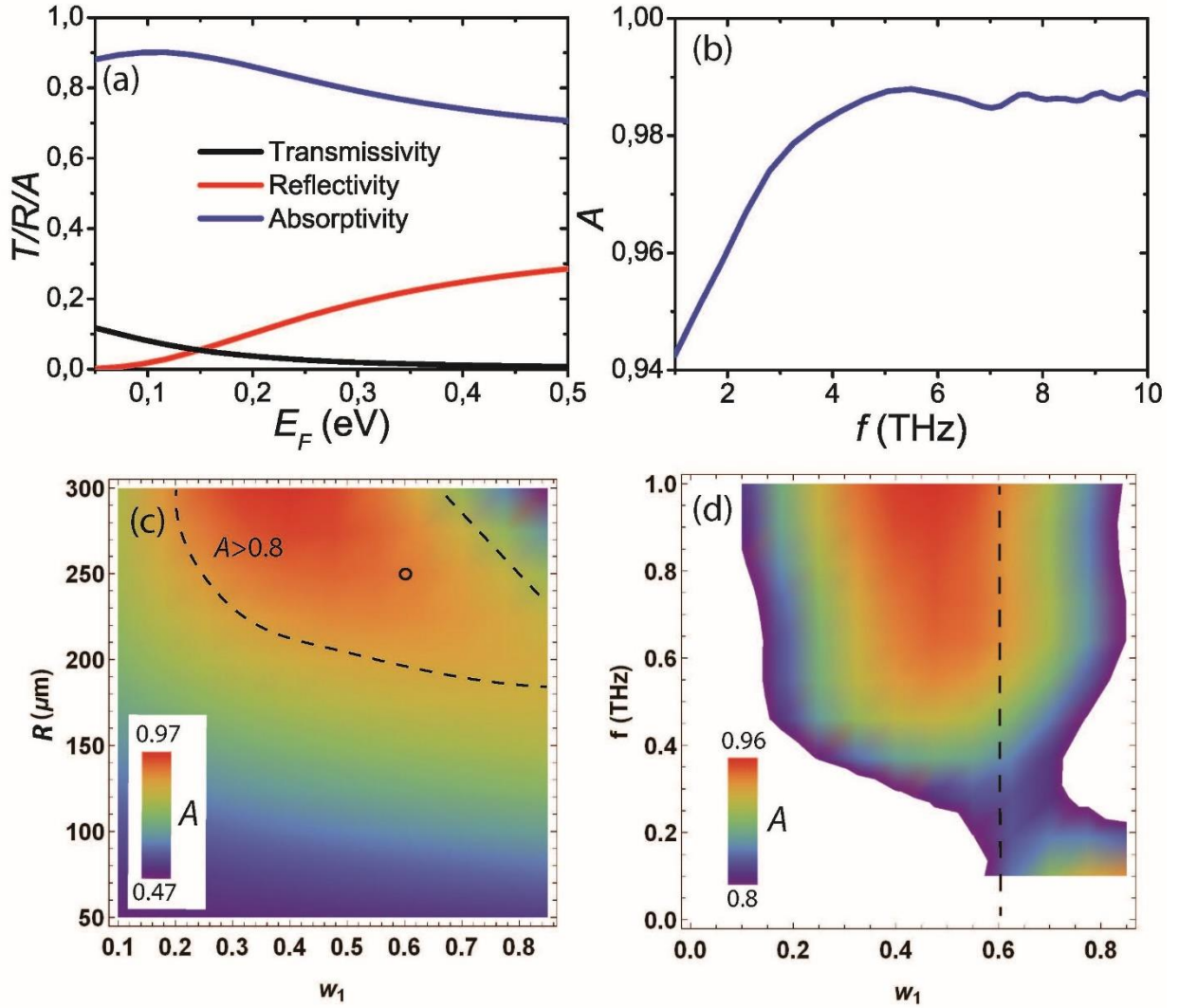
Figure 7. (a) Transmissivity, reflectivity, and absorptivity as functions of the Fermi energy at $f_0 = 0.5$ THz. (b) Absorptivity A vs. frequency at $E_F = 0.1$ eV. Absorptivity as a function of a couple of parameters: (c) $A(w_1, R)$ and (d) $A(w_1, f)$. We adopt parameters as in Fig. 4. In (c), the dashed lines distinguish the area of high absorptivity ($A>0.8$). The circle in (c) and vertical dashed line in (d) mark the experimental parameters.

6 Conclusion

In this paper, we present a novel approach for description of the random metasurfaces. The broken periodicity of meta-atoms array allows us to describe the diffraction problem in terms of the scattering of individual meta-atoms. The developed theory can be applied to any 'random' or non-perfect electromagnetic metasurfaces composed of isotropic, anisotropic, chiral and bianisotropic unit cells, acting in the wavelengths, where the Bragg resonances are suppressed.

We apply this strategy for a random graphene metasurface containing three types of meta-atoms originated from the imperfection of fabrication process (perfect hemisphenes, and hole- and volcano-type defects). Extraordinarily broadband absorbing random graphene metasurface was chosen as a good, experimentally realized, example to show the applicability of a developed diffraction theory and how efficient it might be for optimizing the fabrication / synthesis parameters.

The theory well suits the experimental measurements as demonstrated in Fig. 6 provided that (i) there is no electromagnetic coupling between the meta-atoms and (ii) the number of meta-atoms of each type is large enough to break the periodicity. The developed theory and experimental results show that the free-standing random graphene metasurface exhibits outstanding absorption ability.

The close-to-perfect absorptivity is broadband and highly tolerant to variation of the geometric and material parameters. Thus, the defective fabrication may enhance the absorption performance of the metasurface providing researchers with a broadband absorber in the THz range.

Acknowledgement

References

[1] H.-T. Chen, A.J. Taylor, and N. A. Yu, Review of metasurfaces: physics and applications, Rep. Prog. Phys. **79**, 076401 (2016).

[2] S.B. Glybovski, S.A. Tretyakov, P.A. Belov, Y.S. Kivshar, and C.R. Simovski, Metasurfaces: From microwaves to visible, Physics Reports **634**, 1 (2016).

[3] F. Ding, A. Pors, and S. I. Bozhevolnyi, Gradient metasurfaces: a review of fundamentals and applications, Rep. Prog. Phys. **81**, 026401 (2018).

[4] O. Quevedo-Teruel, H. Chen, A. Díaz-Rubio, G. Gok, A. Grbic, G. Minatti, E. Martini, S. Maci, G.V. Eleftheriades, M. Chen, N.I. Zheludev, N.Papasimakis, S. Choudhury, Z.A. Kudyshev, S. Saha, H. Reddy, A. Boltasseva, V.M. Shalaev, A.V. Kildishev, D. Sievenpiper, C. Caloz, A. Alù, Q. He, L. Zhou, G. Valerio, E. Rajo-Iglesias, Z. Sipus, F. Mesa, R. Rodríguez-Berral, F. Medina, V. Asadchy, S. Tretyakov, and C. Craeye, Roadmap on metasurfaces, J. Opt. **21**, 073002 (2019).

[5] W.T. Chen, A.Y. Zhu, and F. Capasso, Flat optics with dispersion-engineered metasurfaces, Nat. Rev. Materials **5**, 604 (2020).

[6] N. Yu, P. Genevet, M.A. Kats, F. Aieta, J.-P. Tetienne, F. Capasso, and Z. Gaburro, Light propagation with phase discontinuities: generalized laws of reflection and refraction, Science **334**, 333 (2011).

[7] E. Hasman, G. Biener, A. Niv, and V. Kleiner, Space-Variant Polarization Manipulation, Progress in Optics **47**, 215 (2005).

[8] C. Pfeiffer and A. Grbic, Metamaterial Huygens' Surfaces: Tailoring Wave Fronts with Reflectionless Sheets, Phys. Rev. Lett. **110**, 197401 (2013).

[9] B. Sensale-Rodriguez, R. Yan, M. M. Kelly, T. Fang, K. Tahy, W. S. Hwang, D. Jena, L. Liu, and H. G. Xing, Broadband graphene terahertz modulators enabled by intraband transitions, Nat. Commun. **3**, 780 (2012).

[10] H. Chen, W.-B. Lu, Z.-G. Liu, and M.-Y. Geng, Microwave Programmable Graphene Metasurface, ACS Photonics **7**, 1425 (2020).

[11] S.R. Biswas, C.E. Gutiérrez, A. I.-H. Nemilentsau, I.-H. Lee, S.-H. Oh, P. Avouris, and T. Low, Tunable Graphene Metasurface Reflectarray for Cloaking, Illusion, and Focusing, Phys. Rev. Applied **9**, 034021 (2018).

[12] G. Hu, A. Krasnok, Y. Mazor, C.-W. Qiu, and A. Alù, Moiré Hyperbolic Metasurfaces, Nano Lett. **20**, 3217 (2020).

[13] R.-H. Xiong, X.Q. Peng, and J.-S. Li, Graphene-metasurface for wide-incident-angle terahertz absorption, Frontiers of Information Technology & Electronic Engineering **22**, 334 (2021).

[14] S. Lee, H. Heo, and S. Kim, Graphene perfect absorber of ultra-wide bandwidth based on wavelength-insensitive phase matching in prism coupling, Sci. Rep. **9**, 11967 (2019).

[15] X. Li, G. Feng, and S. Lin, Ultra-wideband terahertz absorber based on graphene modulation, Applied Optics **60**, 3170 (2021).

[16] E. Galiffi, J. B. Pendry, and P. A. Huidobro, Broadband tunable THz absorption with singular graphene metasurfaces, ACS Nano **12**(2), 1006 (2018).

[17] M. Dupré, L. Hsu, and B. Kanté, On the design of random metasurface based devices, Sci. Rep. **8**, 7162 (2018).

[18] J. D. Jackson, *Classical Electrodynamics* (John Wiley & Sons, New York, 1999).

[19] M. Baah, A. Paddubskaya, A. Novitsky, N. Valynets, M. Kumar, T. Itkonen, M. Pekkarinen, E. Soboleva, E. Lahderanta, M. Kafesaki, Y. Svirko, and P. Kuzhir, All-graphene perfect broadband THz absorber, Carbon **185**, 709 (2021).

[20] A. Ferreira, J. Viana-Gomes, Y.V. Bludov, V. Pereira, N.M.R. Peres, and A.H. Castro Nero, Faraday effect in graphene enclosed in an optical cavity and the equation of motion method for the study of magneto-optical transport in solids, Phys. Rev. B **84**, 235410 (2011).

[21] A. Paddubskaya, N. Valynets, S. Maksimenko, M. Kumar, M. Baah, M. Pekkarinen, Y. Svirko, G. Valusis, and P. Kuzhir , THz photonics with graphene enhanced polymer hemispheres array, Nanomaterials **11**(10), 2494 (2021).

[22] K. Batrakov, P. Kuzhir, S. Maksimenko, N. Volynets, S. Voronovich, A. Paddubskaya, G. Valusis, T. Kaplas, Y. Svirko, and Ph. Lambin, Enhanced microwave-to-terahertz absorption in Graphene, Appl. Phys. Lett. **108**, 123101 (2016).

[23] N.K. Emani, A.V. Kildishev, V.M. Shalaev, and A. Boltasseva, Graphene: A Dynamic Platform for Electrical Control of Plasmonic Resonance, Nanophotonics **4**, 214 (2015).